Morphological Transitions of a Photoswitchable Aramid Amphiphile Nanostructure

Citation: Kim, Dae-Yoon, Christoff-Tempesta, Ty, Lamour, Guillaume, Zuo, Xiaobing, Ryu, Ki-Hyun et al. 2021. "Morphological Transitions of a Photoswitchable Aramid Amphiphile Nanostructure." Nano Letters, 21 (7).

Published Version: 10.1021/ACS.NANOLETT.0C05048

Publisher: American Chemical Society (ACS)

Permanent Link: https://hdl.handle.net/1721.1/142560

Version: Author's final manuscript: final author’s manuscript post peer review, without publisher’s formatting or copy editing

NANO LETTERS

pubs.acs.org/NanoLett

Letter

Morphological Transitions of a Photoswitchable Aramid Amphiphile Nanostructure

Dae-Yoon Kim,[⊥] Ty Christoff-Tempesta,[⊥] Guillaume Lamour, Xiaobing Zuo, Ki-Hyun Ryu, and Julia H. Ortony*

Cite This: https://doi.org/10.1021/acs.nanolett.0c05048

Read Online

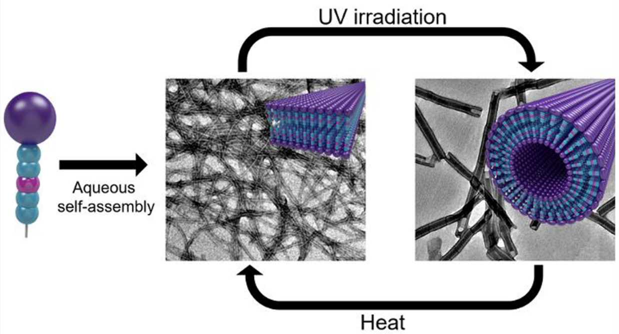

ABSTRACT: Self-assembly of small amphiphilic molecules in water can lead to nanostructures of varying geometries with pristine internal molecular organization. Here we introduce a photoswitchable aramid amphiphile (AA), designed to exhibit extensive hydrogen bonding and robust mechanical properties upon self-assembly, while containing a vinylnitrile group for photoinduced *cis*–*trans* isomerization. We demonstrate spontaneous self-assembly of the vinylnitrile-containing AA in water to form nanoribbons. Upon UV irradiation, *trans*-to-*cis* isomerizations occur concomitantly with a morphological transition from nanoribbons to nanotubes. The nanotube structure persists in water for over six months, stabilized by strong and collective intermolecular interactions. We demonstrate that the nanoribbon-to-nanotube transition is reversible upon heating and that switching between states can be achieved repeatedly. Finally, we use electron microscopy to capture the transition and propose mechanisms for nanoribbon-to-nanotube rearrangement and vice versa. The stability and switchability of photoresponsive AA nanostructures make them viable for a range of future applications.

KEYWORDS: *Small-molecule self-assembly, aramid amphiphile, photoisomerization, nanoribbon, nanotube*

Molecular self-assembly of amphiphilic small molecules in water provides a route to nanostructures with high surface areas and versatile surface chemistries.[1−3] The dimensions of self-assembled nanostructures are determined by the lengths of their constituent molecules; in turn, amphiphilic molecules assemble to form nanostructures with dimensions on the order of 10 nm along at least one axis and high surface areas.[4−6] Further, these architectures readily allow for the inclusion of functional molecules by coassembly, facilitating reactions or recognition events at their surfaces.[7−9] Amphiphilic self-assembly is governed by noncovalent interactions and therefore leads to dynamic and path-dependent morphologies.[10−12] Such materials have shown great promise as biomaterials, where fast conformational dynamics are an important feature,[13−16] and also in the area of systems chemistry, which exploits collective behaviors of ensembles of molecules governed by their dynamic nature.[17]

Imparting photoswitching capabilities within self-assembled small-molecule nanostructures is an important target for introducing new functions. Phototriggers have been combined with amphiphilic self-assembly for a variety of purposes: to liberate surface-bound cell signaling moieties from bioactive nanofiber matrices,[18] to modulate bilayer membrane fluidity,[19] to disrupt the balance of *cis*–*trans* equilibria by selectively arresting one isomer into an assembled structure,[20] to modulate mechanical properties for photolithography and adhesion/lubrication applications,[21] and for photoinitiated synthesis of amphiphiles in water.[22] However, photoisomerization in these systems has generally so far only led to relatively short-lived metastable states, with half-lives ranging from seconds to days.[23] We hypothesize that achieving a morphological transition whose reverse reaction also requires input energy may be accomplished by tuning the intermolecular interaction strengths within the metastable nanostructure.

Though less frequently used, the isomerized products of stilbene-derived chromophores are more stable in contrast to those from conventional azobenzene dyes and can be used to enhance the half-life of a metastable nanostructure.[24−27] Vinylnitrile-based groups—a class of stilbene-derived chromophores—incorporated in a molecular structure can be isomerized by irradiation from the *trans* to *cis* state and spontaneously revert slowly (on the order of minutes to days)

Received: December 28, 2020
Revised: February 24, 2021

at room temperature.[23,28,29] Thus, programming the design of photoresponsive small molecules can allow us to tune molecular self-assembled nanoarchitectures with desirable dimensions and time-stable morphologies.

Here, we investigate the phototriggered isomerization reaction of amphiphiles after self-assembly into strongly cohesive nanoribbons in water. The chemical structure of the small-molecule constituents is designed to exhibit (1) strong and extensive intermolecular interactions and (2) a photoactive moiety known for a dramatic geometric transition upon a 365 nm UV (UVA) light irradiation. This approach is hypothesized to induce molecular isomerization for reversible morphological transitions, with structural stability in both the *trans* and *cis* morphological states.

A strong and extensive network of intermolecular interactions within the nanostructure is achieved by employing aramid amphiphile (AA) molecules. AAs have previously been show to assemble spontaneously in water to form nanoribbons with thicknesses and widths under 10 nm and lengths greater than tens of microns.[30] Within AA nanoribbons, each molecule is fixed in place by six in-register hydrogen bonds propagating down the length of the nanoribbon and $\pi-\pi$ stacking across its width. This network of strong interactions suppresses molecular exchange and migration within assemblies and produces nanoribbons with robust mechanical properties, rivaling silk.[30]

AAs are composed of a hydrophilic headgroup, an aramid structural domain, and a hydrophobic tail (Figure 1a). Here, we design a photoswitchable analogue to the conventional AA molecule which incorporates a vinylnitrile group into the center of the aramid structural domain (Figure 1b). This molecule is designed to similarly form nanoribbons in water but further exhibit a morphological transition upon UVA irradiation. The effect of isomerization of adjacent vinylnitrile groups and the strong intermolecular interactions within the nanostructure are hypothesized to dramatically increase the lifetime of the isomerized product. Compound **1** (Figure 2a) is selected as a control for this experiment for its similar chemical structure and equivalent number of hydrogen bonds as compound **2** (Figure 2d).

Compound **1** is an AA that spontaneously self-assembles in water to form high-aspect-ratio nanoribbons (Figure 2b).

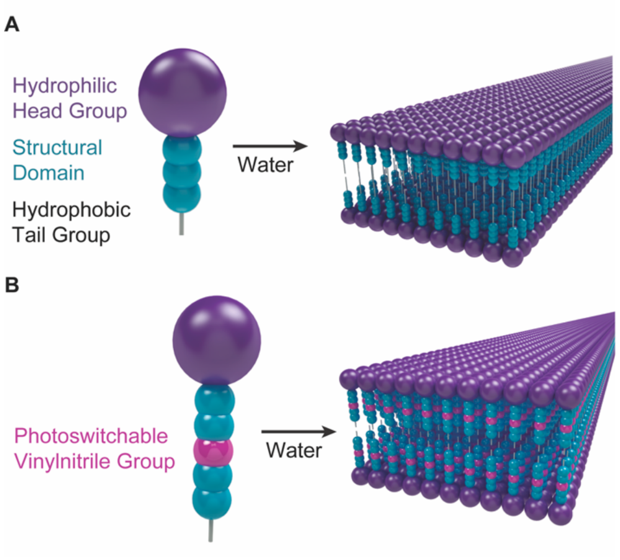

Figure 1. Aramid amphiphiles (AAs) self-assemble in water to form nanoribbons. Their stabilities are bolstered by strong intermolecular hydrogen bonding between adjacent aramid structural domains. (a) Conventional AAs self-assemble in water to form planar nanoribbons with no photo-responsive behavior. (b) Photoresponsive AAs, designed analogously to conventional AAs but with a vinylnitrile moiety in the center of the aramid domain, are designed to assemble into nanoribbons in water with triggerable morphological transitions.

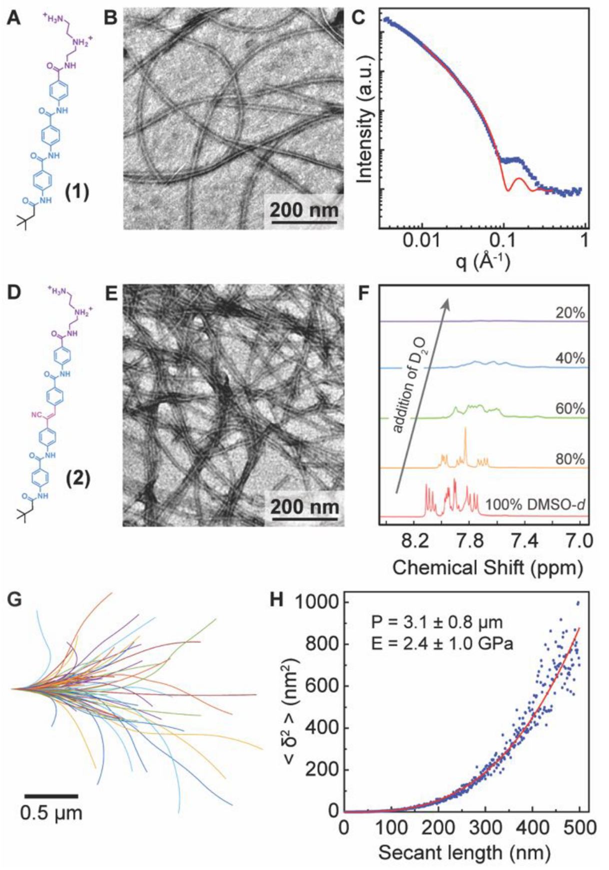

Figure 2. Both conventional and photoswitchable AAs form nanoribbons in water. (a,b) Compound **1** is a conventional AA with a cationic headgroup (purple), aramid structural domain (blue), and short aliphatic tail (black) that spontaneosuly forms nanoribbons with 5.8 nm widths upon assembly in water. (c) Compound **1** nanoribbons are determined to have 3.9 nm thicknesses based on lamellar fitting (red line) to SAXS. (d) Compound **2** incorporates a photoswitchable vinylnitrile moiety (pink) into the aramid amphiphile design. (e) Compound **2** forms nanoribbons mimicking those of compound **1** upon spontaneous assembly in water. (f) The assembly of compound **2** is observed by ^{1}H NMR of the aromatic molecular region as the ratio of D_2O to DMSO-*d* increases. Assembly of the amphiphiles in D_2O results in an upfield proton shift from magnetic shielding and peak broadening from slowing conformational dynamics. (g) Contours of compound **2** nanoribbons (n = 96) are traced from AFM profiles for statistical topographical analysis. (h) Midpoint deviations (δ) from the contour traces of compound **2** nanoribbons are used to derive a Young's modulus of $E = 2.4 \pm 1.0$ GPa from calculating a persistence length, $P = 3.1 \pm 0.8$ μm, by least-squares fitting of a worm-like chain model for semiflexible polymers (red line) to the data. This stiffness value closely matches that of prototypical AAs.[30]

Compound 1 nanoribbons exhibit strong internal cohesion resulting in suppressed exchange dynamics.[10,30] The small-angle X-ray scattering (SAXS) profile of **1** at a concentration of 30 mg/mL is fit (Figure 2c, Figure S13) to determine nanoribbon thickness of 3.9 nm. The widths of **1** nanoribbons is approximated from TEM as 5.8 nm.[31]

Compound **2** is obtained following similar reactions as previously reported.[30] In short, the molecule is built up with alternating carbodiimide-mediated amidation coupling reactions and standard deprotection reactions, and uses the Knoevenagel reaction to obtain the target compound. Detailed synthetic methods are described in Supporting Information Sections S2 and S6. The chemical structures and purities are confirmed by ^{1}H and ^{13}C nuclear magnetic resonance (NMR), matrix-assisted laser desorption and ionization time-of-flight (MALDI-ToF) mass spectrometry, and elemental analysis.

We first seek to understand the self-assembly behavior of compound **2** in water. As previously observed for compound **1**, compound **2** spontaneously forms high-aspect-ratio nanoribbons with lengths on the order of microns upon assembly in water (Figure 2e). Hydrogen bonding between amides in the aramid structural domain is likely the main driving force in forming the elongated nanoribbon structure. $\pi-\pi$ stacking assists in holding the hydrogen bonding sheets laterally, and the local dipole moments of the cyanide can further help to induce side-to-side intermolecular coupling.

Molecular interaction resulting from the self-assembly of **2** in water can be investigated via solvent variation (Figure 2f). Compound **2** is highly soluble in deuterated dimethyl sulfoxide (DMSO-*d*), resulting in a monomeric state. This is observed in the ^{1}H NMR spectra of **2** by well-resolved, sharp peaks, shown for aromatic rings in the structural domain. These proton peaks widen and shift upfield when deuterated water (D_2O) is titrated into the solution. The gradual broadening of these peaks is concomitant with the formation of strong intermolecular interactions and the slowing of conformational dynamics upon self-assembly of **2** in water. The upfield shift of protons results from the tightening of intermolecular distances with assembly that induces a magnetic shielding effect. No nanoribbons or other nanostructures are observed by TEM when **1** or **2** is dissolved in 100% DMSO-*d*.

Compound **1** nanoribbons were previously shown to exhibit a Young's modulus $E = 1.7 \pm 0.7$ GPa.[30] Here, we employ a statistical topographical analysis of nanoribbon contours to determine if incorporating the photoswitchable vinylnitrile moiety impacts the nanoribbons' mechanical properties (SI Section S8). This technique overcomes the lower size bound limitations of direct mechanical measurements, enabling stiffness measurements on nanofilaments with diameters below 10 nm.[32,33] The contours of $n = 96$ compound **2** nanoribbons in water were captured by atomic force microscopy (Figure 2g). Parametric splines were extracted from each contour and used to obtain a nanoribbon persistence length of $P = 3.1 \pm 0.8$ μm, from which a Young's modulus of $E = 2.4 \pm 1.0$ GPa is calculated (Figure 2h).[32,34] This stiffness closely matches the previously reported stiffness for compound **1** nanoribbons,[30] likely resulting from similar intermolecular interaction strengths and hydrogen bond densities between the amphiphiles.

Molecular-scale isomerizations of photoresponsive aromatic molecules result in changes in absorbance that can be detected by UV–vis absorption spectroscopy. As expected, we observe no change in absorbance of aqueous solutions of **1** upon 1 h of irradiation with UVA light (0.1 mg/mL, 1500 mW/cm^2, Figure S18). In contrast, a 0.1 mg/mL solution of compound **2** dissolved in dimethyl sulfoxide (DMSO) shows a dramatic reduction in peak intensity at $\lambda_{max} = 350$ nm under the same conditions (Figure S19). This spectral change indicates that the vinylnitrile *cis* isomer is increased during irradiation with a corresponding decrease in the amount of *trans* isomer (isomer nomenclature discussion in SI Section S4).

Compound **2** assembled in water (0.1 mg/mL) also shows a spectral change after 1 h of irradiation with UVA light similar to that observed in DMSO (Figure 3a). The photochemical reaction rate of **2** in water ($K = 5.44 \times 10^{-2}$/min, Figure 3b) is slightly suppressed compared to its rate in DMSO ($K = 1.10 \times 10^{-1}$/min). In addition, the reduction in peak absorbance intensity corresponding to the photoisomerization is decreased from 80% in DMSO to 67% in water. Changes in the state of soft matter driven by photochemical reactions are sensitive to their local environments, including polarity, viscosity, and light polarization, as well as the strength of intermolecular interactions when photochromic molecules are dissolved or dispersed in solvent.[35] Thus, we infer that the significant change in the molecules' local environments afforded by self-assembly impacts their measured photoisomerization kinetics.

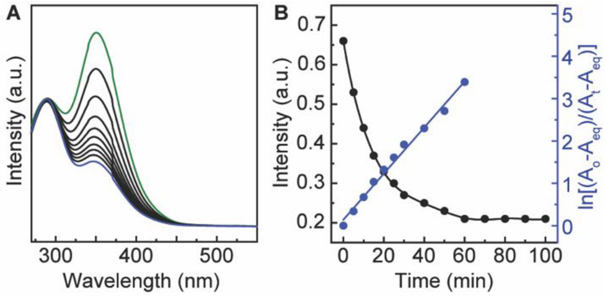

Figure 3. Nanoribbons from compound **2** in water show triggerable isomerization upon UVA irradiation. (a) Compound **2** exhibits a 67% drop in peak absorbance after 1 h of irradiation. The initial state is shown in green, and the photostationary state is shown in blue. (b) Time-dependent absorbance changes upon UVA irradiation of compound **2** are used to create a first-order plot of the *trans* to *cis* isomerization and extract a photoisomerization rate constant of $K = 5.44 \times 10^{-2}$/min.

We verify that nanostructures persist in water after photoisomerization by observing the Tyndall effect in solution. Compound **2** dissolved in DMSO before and after UVA exposure does not exhibit Tyndall scattering (i.e., light scattering upon red laser illumination indicative of the presence of nanostructures), and correspondingly no nanostructures are observed by AFM (Figure S22). Conversely, **2** in water displays significant Tyndall scattering before and after UVA irradiation, indicating the maintenance of nanostructures throughout the photoisomerization (Figure S22).[36] AFM verifies the presence of nanoribbons before UVA irradiation and suggests a different nanotube structure afterward. We further demonstrate that the morphological transition of compound **2** in water is facilitated when the intensity of UVA light is increased (Figure S20).

With this information, we seek to understand the morphology of the *cis*-rich compound **2** assembly. We observe that compound **2** nanoribbons convert into nanotubes as the vinylnitrile moiety undergoes a *trans*-to-*cis* isomerization.

Initially, compound **2** nanoribbons mimic the structure of nanoribbons **1**, as shown by TEM and SAXS (Figures 2e and 4a). The SAXS profile of an aqueous solution of **2** was best fit to a rectangular prism model, returning nanoribbon dimensions of 4.7 nm in thickness and 5.4 nm in width (Figure S14).[37] Upon UVA irradiation of an aqueous solution of compound **2** nanoribbons for 1 h, the nanoribbons converted into nanotubes with a shell thickness comparable to the nanoribbon thickness (Figure 4b). The SAXS profile of the aqueous nanotube solution was fit to a hollow cylinder model with a 19.4 nm core diameter and a 6.1 nm shell thickness (Figure 4c, Figure S15).[38]

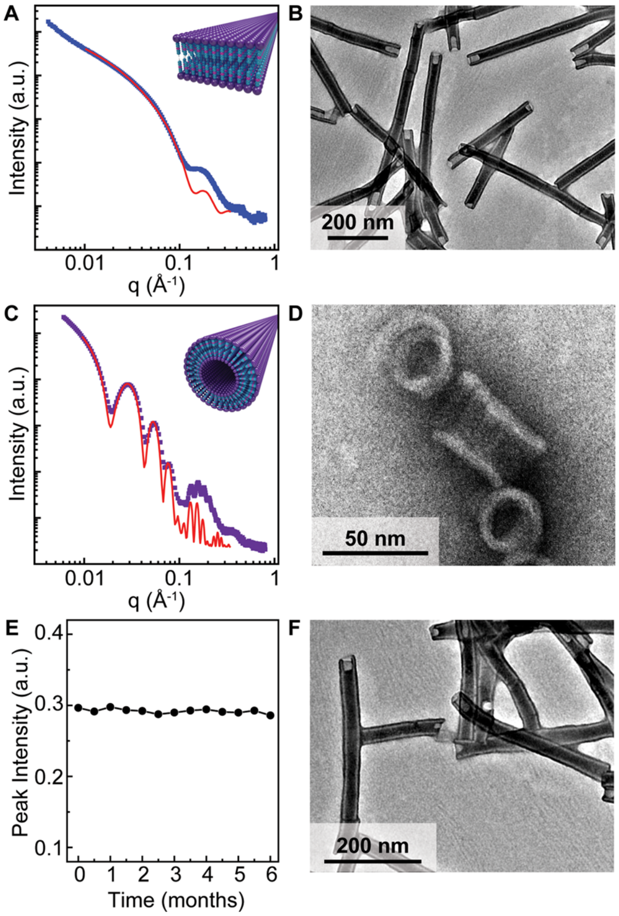

Figure 4. Compound **2** nanoribbons transition into nanotubes upon UVA irradiation and maintain their isomerized structure for at least six months. (a) Fitting of a rectangular prism model to SAXS of compound **2** nanoribbons is used to extract a 4.7 nm × 5.4 nm cross-section. (b) After 1 h of UVA irradiation, compound **2** nanoribbons convert into nanotubes observable by TEM. (c) Fitting of a hollow cylinder model to SAXS of compound **2** nanotubes reveals a 6.1 nm shell thickness and 19.4 nm core diameter. (d) Planar **2** nanoribbons coil under UVA light to form tight spirals in the nanoribbon to nanotube transition. The edges of the spirals fuse to form the observed final nanotube structure. (e) UV−vis absorption spectroscopy shows the maintenance of the same peak absorbance intensity corresponding to the *cis* state for six months, measured in half-month intervals. (f) Representative TEM of compound **2** nanotubes six months after UVA irradiation shows no evidence of nanoribbon formation.

The structural transition demonstrated in Figures 4a−c led us to investigate the mechanism of nanoribbon-to-nanotube morphological conversion in order to further understand the switching phenomena. We irradiated nanoribbons of **2** for just 10 min, rather than the typical irradiation time corresponding to the PSS, to capture its intermediate state. TEM of the solution at this time point shows an intermediate coiled ribbon nanostructure (Figure 4d). By comparing the dimensions of the nanoribbon coils to those of the nanotube itself, we can conclude that the photochemical reaction of amphiphiles within the nanoribbon assembly results in twisting of the nanoribbons to form tight coils, which then fuse to yield nanotubes. For context, folding of supramolecular nanoribbons into helical shapes without fusing,[39,40] toroid stacking to form tubular or helical structures,[41] and light-induced tubular disassembly[42] have been previously reported, but the mechanism shown here in the case of aramid amphiphiles has not previously been demonstrated as a response to photoisomerization in supramolecular assemblies. Similar mechanisms have been observed for chiral amphiphiles, bent core liquid crystals, and discotic polyaromatic hydrocarbons.[43−45]

The formation of lamellar nanoribbons by the *trans* state of **2** is driven by dense intermolecular interactions between amphiphilic molecules. Compound **2** nanoribbons are constructed from layers of molecules aligned normal to the nanoribbon length axis. In the *trans* state, the molecules have a rod-like geometry, providing a feasible path for the formation of a nanoribbon morphology. Upon UVA irradiation for conversion of **2** to the *cis* state, the molecules take on a bent-shape geometry and flexible conformation, resulting in local reorganization to compensate for space requirements. Diffraction on the subnanometer length scale provides local molecular packing information, so we perform 1D wide-angle X-ray diffraction (WAXD) on lyophilized samples of compound **2** nanostructures to elucidate this effect.[46] Weakening and broadening of sharp reflection peaks after UVA irradiation indicate that long-range molecular and short-range positional orders are partially disrupted compared to the *trans* state (Figure S23). To maintain favorable interactions, we infer that the hydrophilic cationic head groups orient toward their aqueous environment, inducing curvature to the assembly.[47] Torsion induced by this curvature leads to the nanoribbon twisting, which ultimately fuses at the energetically unfavorable hydrophobic edges to produce nanotubes.[48]

Reaching the PSS of **2** is similar to typical light-driven responses, but in contrast to that of previously reported materials, the isomerized product of **2** remains unchanged for several months after turning off UVA light (Figures 4e,f). The strongly interacting nature of compound **2** molecules in an assembled state, aided by hydrogen bonding and $\pi-\pi$ stacking in the aramid structural domain, drastically enhances their activation barrier for *cis*-to-*trans* isomerization, thereby increasing the nanotube lifetime. Consequently, we observe no nanotube-to-nanoribbon reversal at time points up to six months by UV−vis spectroscopy and TEM.

Finally, we investigated whether the isomerization reaction and consequent morphological transition are reversible by providing sufficient thermal energy for the vinylnitrile to revert to its *trans* ground state. Unable to overcome the activation barrier for reversibility at room temperature, we hypothesized that adding thermal energy could induce the reverse reaction as it increases the conformational dynamics within the nanostructure, facilitating the one-bond-flip isomerization reaction from *cis* to *trans*.[49,50] Upon heating a solution of compound **2** nanoribbons to 80 °C for 1 h and cooling slowly, we observe a recovery in UV−vis absorbance to its original peak value. This heating and irradiation process can be repeated at least five times, indicating that the isomerization transition can be repeatedly performed on the nanostructures without loss (Figure 5a, Figure S21). The nanotube heating process fully regenerates nanoribbons with the same dimensions as their original assembled state (Figures 5b,c, Figure S16).

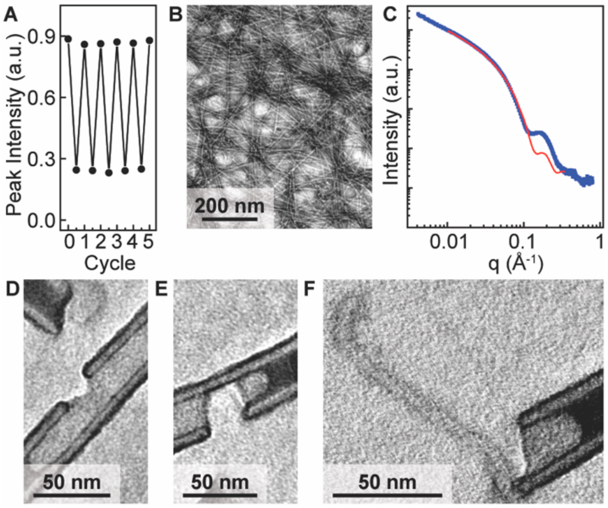

Figure 5. Photoisomerization of compound **2** from nanoribbons to nanotubes is reversed by heating at 80 °C for 1 h. (a) **2** isomerization is cyclically modulated over five cycles from repeated UVA irradiation and heating, as captured by tracking the peak absorbance intensity by UV−vis spectroscopy. (b) Representative TEM of compound **2** nanoribbons after 1 h of heating compound **2** nanotubes at 80 °C. (c) SAXS of compound **2** nanoribbons after heating from the nanotube morphology shows a return to its original dimensions, based on a rectangular prism fit (red). (d−f) Upon heating, compound **2** nanotubes rupture under torsional strain from isomerization, releasing nanoribbons that resemble the initial assemblies.

We again sought to capture the intermediate state of the morphological transition occurring with the reverse isomerization. The vinylnitrile *cis*-to-*trans* isomerization induces strain that causes rupture of the nanotube (Figure 5d). This rupture propagates across the nanotube to sciss the nanostructure (Figure 5e) and enables nanoribbon formation by unraveling of the nanotube at the interfaces (Figure 5f).

Here, we presented a photoresponsive aramid amphiphile (AA) platform for molecular self-assembly into supramolecular nanostructures. We demonstrate that the *trans*-to-*cis* photoisomerization of constituent molecules triggers a morphological transition from nanoribbons to nanotubes. The nanotube state exhibits a long lifetime, especially for vinylnitrile moieties, of at least six months, achieved by employing the AA motif, a structure that exploits strong and extensive intermolecular interactions. We further demonstrated the reversibility of the morphological transition by providing sufficient thermal energy to induce the *cis*-to-*trans* conversion and recover the initial nanoribbon morphology. We captured the intermediate states of both morphological transitions to reveal their mechanisms: nanoribbon coiling and edge-to-edge fusion to form nanotubes and nanotube fracture to release nanoribbons from the interfaces. This self-assembly platform could meet pressing challenges in responsive nanomaterial design by combining high nanostructure stability and long excited-state lifetimes with the capability to undergo phototriggered morphological transitions.

■ ASSOCIATED CONTENT

Supporting Information

The Supporting Information is available free of charge at https://pubs.acs.org/doi/10.1021/acs.nanolett.0c05048.

> Materials, synthesis, sample preparation, isomer naming conventions, characterization details, SAXS fitting, statistical topographical analysis of nanoribbon contours, UV−vis controls and experiments, Tyndall effect, and proposed packing of **2** amphiphiles (PDF)

■ AUTHOR INFORMATION

Corresponding Author

Julia H. Ortony − *Department of Materials Science and Engineering, Massachusetts Institute of Technology, Cambridge, Massachusetts 02139, United States;* orcid.org/0000-0001-7446-6207; Email: ortony@mit.edu

Authors

Dae-Yoon Kim − *Department of Materials Science and Engineering, Massachusetts Institute of Technology, Cambridge, Massachusetts 02139, United States; Institute of Advanced Composite Materials, Korea Institute of Science and Technology, Bondong, JB 55324, Korea*
Ty Christoff-Tempesta − *Department of Materials Science and Engineering, Massachusetts Institute of Technology, Cambridge, Massachusetts 02139, United States*
Guillaume Lamour − *LAMBE, Université Paris-Saclay, University of Evry, CNRS, Evry-Courcouronnes, France;* orcid.org/0000-0002-9331-5532
Xiaobing Zuo − *X-ray Science Division, Advanced Photon Source, Argonne National Laboratory, Argonne, Illinois 60439, United States*
Ki-Hyun Ryu − *Institute of Advanced Composite Materials, Korea Institute of Science and Technology, Bondong, JB 55324, Korea*

Complete contact information is available at: https://pubs.acs.org/10.1021/acs.nanolett.0c05048

Author Contributions

⊥D.-Y.K. and T.C.-T. contributed equally.

Funding

This material is based upon work supported by the National Science Foundation under Grant No. CHE-1945500. This work was supported in part by the Professor Amar G. Bose Research Grant Program and the Abdul Latif Jameel Water and Food Systems Lab. D.-Y.K. acknowledges the support of the Open Research Program (2E31332) of the Korea Institute of Science and Technology and the National Research Foundation of Korea (2021R1R1R1004226). T.C.-T. acknowledges the National Science Foundation Graduate Research Fellowship Program under Grant No. 1122374. G.L. acknowledges support from the University of Evry Paris-Saclay.

Notes

The authors declare no competing financial interest.

■ ACKNOWLEDGMENTS

This work made use of the MRSEC Shared Experimental Facilities at MIT supported by the National Science Foundation under award number DMR-14-19807 and the MIT Department of Chemistry Instrumentation Facility (DCIF). X-ray scattering measurements were performed at beamline 12-ID-B of the Advanced Photon Source, a U.S. Department of Energy (DOE) Office of Science User Facility operated for the DOE Office of Science by Argonne National Laboratory under Contract No. DE-AC02-06CH11357.

■ ABBREVIATIONS

AA, aramid amphiphile; AFM, atomic force microscopy; DMSO, dimethyl sulfoxide; D_2O, deuterated water; DMSO-d, deuterated dimethyl sulfoxide; NMR, nuclear magnetic resonance; PSS, photostationary state; SAXS, small-angle X-ray scattering; TEM, transition electron microscopy; UV−vis, ultraviolet−visible

■ REFERENCES

(1) Whitesides, G. M.; Mathias, J. P.; Seto, C. T. Molecular self-assembly and nanochemistry: a chemical strategy for the synthesis of nanostructures. *Science* **1991**, *254* (5036), 1312−1319.

(2) Aida, T.; Meijer, E.; Stupp, S. I. Functional supramolecular polymers. *Science* **2012**, *335* (6070), 813−817.

(3) Meng, Q.; Kou, Y.; Ma, X.; Liang, Y.; Guo, L.; Ni, C.; Liu, K. Tunable Self-Assembled Peptide Amphiphile Nanostructures. *Langmuir* **2012**, *28* (11), 5017−5022.

(4) Cui, H.; Webber, M. J.; Stupp, S. I. Self-assembly of peptide amphiphiles: From molecules to nanostructures to biomaterials. *Biopolymers* **2010**, *94* (1), 1−18.

(5) Fong, C.; Le, T.; Drummond, C. J. Lyotropic liquid crystal engineering-ordered nanostructured small molecule amphiphile self-assembly materials by design. *Chem. Soc. Rev.* **2012**, *41* (3), 1297−1322.

(6) Lis, L.; McAlister, d.; Fuller, N.; Rand, R.; Parsegian, V. Interactions between neutral phospholipid bilayer membranes. *Biophys. J.* **1982**, *37* (3), 657.

(7) Rao, K. V.; George, S. J. Supramolecular Alternate Co-Assembly through a Non-Covalent Amphiphilic Design: Conducting Nanotubes with a Mixed D-A Structure. *Chem. - Eur. J.* **2012**, *18* (45), 14286−14291.

(8) Xu, Z.; Jia, S.; Wang, W.; Yuan, Z.; Ravoo, B. J.; Guo, D.-S. Heteromultivalent peptide recognition by co-assembly of cyclodextrin and calixarene amphiphiles enables inhibition of amyloid fibrillation. *Nat. Chem.* **2019**, *11* (1), 86−93.

(9) Silva, G. A.; Czeisler, C.; Niece, K. L.; Beniash, E.; Harrington, D. A.; Kessler, J. A.; Stupp, S. I. Selective differentiation of neural progenitor cells by high-epitope density nanofibers. *Science* **2004**, *303* (5662), 1352−1355.

(10) Ortony, J. H.; Newcomb, C. J.; Matson, J. B.; Palmer, L. C.; Doan, P. E.; Hoffman, B. M.; Stupp, S. I. Internal dynamics of a supramolecular nanofibre. *Nat. Mater.* **2014**, *13* (8), 812.

(11) Nieh, M.-P.; Raghunathan, V. A.; Kline, S. R.; Harroun, T. A.; Huang, C.-Y.; Pencer, J.; Katsaras, J. Spontaneously formed unilamellar vesicles with path-dependent size distribution. *Langmuir* **2005**, *21* (15), 6656−6661.

(12) Korevaar, P. A.; Newcomb, C. J.; Meijer, E. W.; Stupp, S. I. Pathway Selection in Peptide Amphiphile Assembly. *J. Am. Chem. Soc.* **2014**, *136* (24), 8540−8543.

(13) Zhang, S. Fabrication of novel biomaterials through molecular self-assembly. *Nat. Biotechnol.* **2003**, *21* (10), 1171.

(14) Christoff-Tempesta, T.; Lew, A. J.; Ortony, J. H. Beyond covalent crosslinks: applications of supramolecular gels. *Gels* **2018**, *4* (2), 40.

(15) Dong, R.; Zhou, Y.; Huang, X.; Zhu, X.; Lu, Y.; Shen, J. Functional supramolecular polymers for biomedical applications. *Adv. Mater.* **2015**, *27* (3), 498−526.

(16) Sun, L.; Zheng, C.; Webster, T. J. Self-assembled peptide nanomaterials for biomedical applications: promises and pitfalls. *Int. J. Nanomed.* **2017**, *12*, 73.

(17) Zelzer, M.; Ulijn, R. V. Next-generation peptide nanomaterials: molecular networks, interfaces and supramolecular functionality. *Chem. Soc. Rev.* **2010**, *39* (9), 3351−3357.

(18) Sur, S.; Matson, J. B.; Webber, M. J.; Newcomb, C. J.; Stupp, S. I. Photodynamic control of bioactivity in a nanofiber matrix. *ACS Nano* **2012**, *6* (12), 10776−10785.

(19) Urban, P.; Pritzl, S. D.; Ober, M. F.; Dirscherl, C. F.; Pernpeintner, C.; Konrad, D. B.; Frank, J. A.; Trauner, D.; Nickel, B.; Lohmueller, T. A Lipid Photoswitch Controls Fluidity in Supported Bilayer Membranes. *Langmuir* **2020**, *36* (10), 2629−2634.

(20) Wu, Z.; Xue, R.; Xie, M.; Wang, X.; Liu, Z.; Drechsler, M.; Huang, J.; Yan, Y. Self-Assembly-Triggered Cis-to-Trans Conversion of Azobenzene Compounds. *J. Phys. Chem. Lett.* **2018**, *9* (1), 163−169.

(21) Zha, R. H.; Vantomme, G.; Berrocal, J. A.; Gosens, R.; de Waal, B.; Meskers, S.; Meijer, E. W. Photoswitchable Nanomaterials Based on Hierarchically Organized Siloxane Oligomers. *Adv. Funct. Mater.* **2018**, *28* (1), 1703952.

(22) Maity, C.; Hendriksen, W. E.; van Esch, J. H.; Eelkema, R. Spatial structuring of a supramolecular hydrogel by using a visible-light triggered catalyst. *Angew. Chem., Int. Ed.* **2015**, *54* (3), 998−1001.

(23) Kathan, M.; Hecht, S. Photoswitchable molecules as key ingredients to drive systems away from the global thermodynamic minimum. *Chem. Soc. Rev.* **2017**, *46* (18), 5536−5550.

(24) Gegiou, D.; Muszkat, K.; Fischer, E. Temperature dependence of photoisomerization. V. Effect of substituents on the photo-isomerization of stilbenes and azobenzenes. *J. Am. Chem. Soc.* **1968**, *90* (15), 3907−3918.

(25) Dyck, R. H.; McClure, D. S. Ultraviolet spectra of stilbene, p-monohalogen stilbenes, and azobenzene and the trans to cis photoisomerization process. *J. Chem. Phys.* **1962**, *36* (9), 2326−2345.

(26) Zhu, H.; Shangguan, L.; Xia, D.; Mondal, J. H.; Shi, B. Control on the photo-responsive assembly of a stilbene-containing amphiphile by using pillar [5] arene-based host-guest interactions. *Nanoscale* **2017**, *9* (26), 8913−8917.

(27) Bléger, D.; Schwarz, J.; Brouwer, A. M.; Hecht, S. o-Fluoroazobenzenes as readily synthesized photoswitches offering nearly quantitative two-way isomerization with visible light. *J. Am. Chem. Soc.* **2012**, *134* (51), 20597−20600.

(28) Yao, X.; Li, T.; Wang, J.; Ma, X.; Tian, H. Recent progress in photoswitchable supramolecular self-assembling systems. *Adv. Opt. Mater.* **2016**, *4* (9), 1322−1349.

(29) Choi, S.; Park, S. H.; Ziganshina, A. Y.; Ko, Y. H.; Lee, J. W.; Kim, K. A stable cis-stilbene derivative encapsulated in cucurbit [7] uril. *Chem. Commun.* **2003**, No. 17, 2176−2177.

(30) Christoff-Tempesta, T.; Cho, Y.; Kim, D.-Y.; Geri, M.; Lamour, G.; Lew, A. J.; Zuo, X.; Lindemann, W. R.; Ortony, J. H. Self-assembly of aramid amphiphiles into ultra-stable nanoribbons and aligned nanoribbon threads. *Nat. Nanotechnol.* **2021**, DOI: 10.1038/s41565-020-00840-w.

(31) Nallet, F.; Laversanne, R.; Roux, D. Modelling X-ray or neutron scattering spectra of lyotropic lamellar phases: interplay between form and structure factors. *J. Phys. II* **1993**, *3* (4), 487−502.

(32) Knowles, T. P.; Fitzpatrick, A. W.; Meehan, S.; Mott, H. R.; Vendruscolo, M.; Dobson, C. M.; Welland, M. E. Role of intermolecular forces in defining material properties of protein nanofibrils. *Science* **2007**, *318* (5858), 1900−1903.

(33) Nassar, R.; Wong, E.; Gsponer, J. r.; Lamour, G. Inverse correlation between amyloid stiffness and size. *J. Am. Chem. Soc.* **2019**, *141* (1), 58−61.

(34) Lamour, G.; Kirkegaard, J. B.; Li, H.; Knowles, T. P.; Gsponer, J. Easyworm: an open-source software tool to determine the

mechanical properties of worm-like chains. *Source code for biology and medicine* **2014**, *9* (1), 1−6.

(35) Uchida, E.; Sakaki, K.; Nakamura, Y.; Azumi, R.; Hirai, Y.; Akiyama, H.; Yoshida, M.; Norikane, Y. Control of the orientation and photoinduced phase transitions of macrocyclic azobenzene. *Chem. - Eur. J.* **2013**, *19* (51), 17391−17397.

(36) Levchuk, I.; Hou, Y.; Gruber, M.; Brandl, M.; Herre, P.; Tang, X.; Hoegl, F.; Batentschuk, M.; Osvet, A.; Hock, R.; et al. Deciphering the role of impurities in methylammonium iodide and their impact on the performance of perovskite solar cells. *Adv. Mater. Interfaces* **2016**, *3* (22), 1600593.

(37) Nayuk, R.; Huber, K. Formfactors of Hollow and Massive Rectangular Parallelepipeds at Variable Degree of Anisometry. *Z. Phys. Chem.* **2012**, *226* (7−8), 837−854.

(38) Feigin, L.; Svergun, D. I. *Structure analysis by small-angle X-ray and neutron scattering*; Springer: 1987; Vol. *1*.

(39) Adhikari, B.; Yamada, Y.; Yamauchi, M.; Wakita, K.; Lin, X.; Aratsu, K.; Ohba, T.; Karatsu, T.; Hollamby, M. J.; Shimizu, N.; Takagi, H.; Haruki, R.; Adachi, S.-i.; Yagai, S. Light-induced unfolding and refolding of supramolecular polymer nanofibres. *Nat. Commun.* **2017**, *8* (1), 15254.

(40) Prabhu, D. D.; Aratsu, K.; Kitamoto, Y.; Ouchi, H.; Ohba, T.; Hollamby, M. J.; Shimizu, N.; Takagi, H.; Haruki, R.; Adachi, S.-i.; Yagai, S. Self-folding of supramolecular polymers into bioinspired topology. *Science Advances* **2018**, *4* (9), No. eaat8466.

(41) Wang, H.; Lee, M. Switching between Stacked Toroids and Helical Supramolecular Polymers in Aqueous Nanotubules. *Macromol. Rapid Commun.* **2020**, *41* (11), 2000138.

(42) Fredy, J. W.; Méndez-Ardoy, A.; Kwangmettatam, S.; Bochicchio, D.; Matt, B.; Stuart, M. C. A.; Huskens, J.; Katsonis, N.; Pavan, G. M.; Kudernac, T. Molecular photoswitches mediating the strain-driven disassembly of supramolecular tubules. *Proc. Natl. Acad. Sci. U. S. A.* **2017**, *114* (45), 11850−11855.

(43) Ziserman, L.; Lee, H.-Y.; Raghavan, S. R.; Mor, A.; Danino, D. Unraveling the mechanism of nanotube formation by chiral self-assembly of amphiphiles. *J. Am. Chem. Soc.* **2011**, *133* (8), 2511−2517.

(44) Wu, D.; Zhi, L.; Bodwell, G. J.; Cui, G.; Tsao, N.; Müllen, K. Self-assembly of positively charged discotic PAHs: from nanofibers to nanotubes. *Angew. Chem., Int. Ed.* **2007**, *46* (28), 5417−5420.

(45) Kim, D.-Y.; Yoon, W.-J.; Choi, Y.-J.; Lim, S.-I.; Koo, J.; Jeong, K.-U. Photoresponsive chiral molecular crystal for light-directing nanostructures. *J. Mater. Chem. C* **2018**, *6* (45), 12314−12320.

(46) Choi, Y.-J.; Jung, D.; Lim, S.-I.; Yoon, W.-J.; Kim, D.-Y.; Jeong, K.-U. Diacetylene-Functionalized Dendrons: Self-Assembled and Photopolymerized Three-Dimensional Networks for Advanced Self-Healing and Wringing Soft Materials. *ACS Appl. Mater. Interfaces* **2020**, *12* (29), 33239−33245.

(47) Shadpour, S.; Nemati, A.; Boyd, N. J.; Li, L.; Prévôt, M. E.; Wakerlin, S. L.; Vanegas, J. P.; Salamończyk, M.; Hegmann, E.; Zhu, C.; et al. Heliconical-layered nanocylinders (HLNCs)-hierarchical self-assembly in a unique B4 phase liquid crystal morphology. *Mater. Horiz.* **2019**, *6* (5), 959−968.

(48) Cano, M.; Sánchez-Ferrer, A.; Serrano, J. L.; Gimeno, N.; Ros, M. B. Supramolecular Architectures from Bent-Core Dendritic Molecules. *Angew. Chem.* **2014**, *126* (49), 13667−13671.

(49) Zhu, L.; Li, X.; Zhang, Q.; Ma, X.; Li, M.; Zhang, H.; Luo, Z.; Ågren, H.; Zhao, Y. Unimolecular photoconversion of multicolor luminescence on hierarchical self-assemblies. *J. Am. Chem. Soc.* **2013**, *135* (13), 5175−5182.

(50) Chung, J. W.; Yoon, S.-J.; An, B.-K.; Park, S. Y. High-contrast on/off fluorescence switching via reversible E-Z isomerization of diphenylstilbene containing the α-cyanostilbenic moiety. *J. Phys. Chem. C* **2013**, *117* (21), 11285−11291.

https://doi.org/10.1021/acs.nanolett.0c05048

Supporting Information for

Morphological transitions of a photoswitchable aramid amphiphile nanostructure

Dae-Yoon Kim[1,2†], Ty Christoff-Tempesta[1†], Guillaume Lamour[3],
Xiaobing Zuo[4], Ki-Hyun Ryu[2], Julia H. Ortony[1*]

[1] Department of Materials Science and Engineering, Massachusetts Institute of Technology, Cambridge, MA 02139, USA.

[2] Institute of Advanced Composite Materials, Korea Institute of Science and Technology, Bondong, JB 55324, Korea.

[3] LAMBE, Université Paris-Saclay, University of Evry, CNRS, Evry-Courcouronnes, France

[4] X-ray Science Division, Advanced Photon Source, Argonne National Laboratory, Argonne, IL 60439, USA.

[†] These authors contributed equally.

[*] Correspondence to: ortony@mit.edu.

Contents:

S1. Materials

Methyl 4-aminobenzoate (Sigma Aldrich, 98%), 3,3-dimethylbutyric acid (Sigma Aldrich, 98%), 4-aminobenzyl cyanide (Sigma Aldrich, 99%), methyl 4-formylbenzoate (Sigma Aldrich, 99%), 1,4-bis-Boc-1,4,7-triazaheptane (Chem Impex, 99%), 1-ethyl-3-(3-dimethylaminopropyl)carbodiimide hydrochloride (EDC, TCI Chemicals, 98%), 4-dimethylaminopyridine (DMAP, TCI Chemicals, 99%), lithium hydroxide (LiOH, Alfa Aesar, 98%), potassium hydroxide (KOH, Alfa Aesar, 98%), hydrochloric acid (HCl, Alfa Aesar, 37%), trifluoroacetic acid (TFA, Alfa Aesar, 99%), diethylether (DEE, Acros Organics, 99%), tetrahydrofuran (THF, Acros Organics, 99%), ethyl acetate (EA, Acros Organics, 99%), hexane (HEX, Acros Organics, 99%), methanol (MeOH, Acros Organics, 99%), ethanol (EtOH, Acros Organics, 99%), dichloromethane (DCM, Acros Organics, 99%), and dimethylformamide (DMF, Acros Organics, 99%) were used as received without further purification.

S2. Synthesis

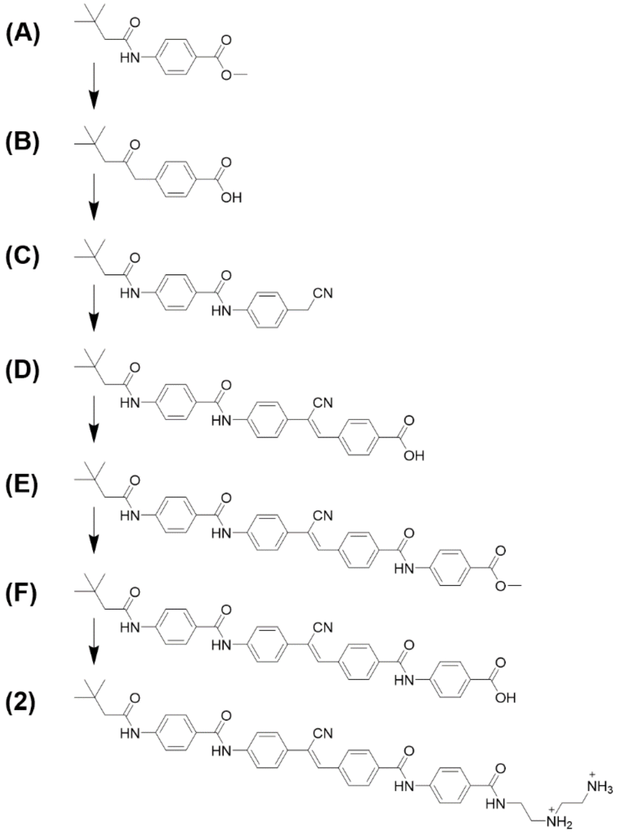

Figure S1. Synthetic route to obtain the photoresponsive aramid amphiphile **2**.

Methyl 4-(3,3-dimethylbutanamido)benzoate (compound **A**): A solution of methyl 4-aminobenzoate (5.5 mmol), 3,3-dimethylbutyric acid (8.3 mmol), EDC (16.5 mmol), and DMAP (16.5 mmol) in DCM (40 mL) was stirred at room temperature for 24 h. The solution was washed with deionized water after the reaction and then extracted in DCM. The organic layer was purified by performing column chromatography with silica gel using EA:HEX = 1:1 as eluent. Yield: 81%. ^{1}H NMR (400 MHz, DMSO-*d*): δ = 7.92 (d, 2H), 7.73 (d, 2H), 3.82 (s, 3H), 2.27 (s, 2H), 1.07 (s, 9H) ppm.

4-(3,3-Dimethylbutanamido)benzoic acid (compound **B**): 10 M LiOH (5 mL) was added to a stirred solution of compound **A** (2.1 mmol) in EtOH (20 mL). The mixture was heated to 70 °C for 6 h, and then neutralized with 1M HCl solution. The precipitate was obtained by filtration and washed with water several times. The crude product was purified by reprecipitation from chloroform and methanol, and then dried under vacuum. Yield: 99%. ^{1}H NMR (400 MHz, DMSO-*d*): δ = 7.87 (d, 2H), 7.71 (d, 2H), 2.23 (s, 2H), 1.03 (s, 9H) ppm.

N-(4-(cyanomethyl)phenyl)-4-(3,3-dimethylbutanamido)benzamide (compound **C**): EDC (6.5 mmol) and DMAP (6.5 mmol) were added to a solution of compound **B** (2.1 mmol) in DMF (20 mL). After stirring at room temperature for 20 min, 4-aminobenzyl cyanide (6.5 mmol) was added as a solid and the solution was sonicated in an ultrasound bath until a clear solution was obtained. The solution was stirred for 24 h at room temperature. A precipitate formed after addition of distilled water (40 mL), which was was collected by filtration and purified by washing with copious MeOH. Yield: 79%. ^{1}H NMR (400 MHz, DMSO-*d*): δ = 7.94 (d, 2H), 7.84 (d, 2H), 7.72 (d, 2H), 7.34 (d, 2H), 4.05 (s, 2H), 2,27 (s, 2H), 1.03 (s, 9H) ppm.

(*Z*)-4-(2-cyano-2-(4-(4-(3,3-dimethylbutanamido)benzamido)phenyl)vinyl)benzoic-acid (compound **D**): Compound **C** (1.6 mmol) and methyl 4-formylbenzoate (1.8 mmol) were dissolved in EtOH (40 mL) and THF (30 mL). The solution was heated in reflux under a nitrogen atmosphere, and KOH (10.3 mmol) was carefully added. The reaction mixture was cooled to room temperature after 24 h. 6M HCl solution was added to form a yellow precipitate which was filtered and washed with DCM. Yield: 88%. ^{1}H NMR (400 MHz, DMSO-*d*): δ = 8.07 (m, 3H), 8.03 (d, 2H), 7.95 (d, 4H), 7.81 (d, 2H), 7.75 (d, 2H), 2.24 (s, 2H), 1.04 (s, 9H) ppm.

Methyl (*Z*)-4-(4-(2-cyano-2-(4-(4-(3,3-dimethylbutanamido)benzamido)phenyl)-vinyl)benzamido)benzoate (compound **E**): A solution of compound **D** (0.6 mmol) in DMF (20 mL) was added to a solution of methyl 4-aminobenzoate (1.8 mmol), EDC (1.8 mmol), and

DMAP (1.8 mmol) in DCM (20 mL). After stirring the mixture for 24 h at room temperature, the solvent was evaporated under reduced pressure. The product was obtained after washing with MeOH and drying. Yield: 83%. ^{1}H NMR (400 MHz, DMSO-*d*): δ = 8.11 (m, 3H), 8.06 (d, 2H), 7.99 (m, 8H), 7.83 (d, 2H), 7.75 (d, 2H), 3.79 (s, 3H), 2.24 (s, 2H), 1.05 (s, 9H) ppm.

(*Z*)-4-(4-(2-cyano-2-(4-(4-(3,3-dimethylbutanamido)benzamido)phenyl)vinyl)benzamido)benzoic acid (compound **F**): 10 M LiOH (10 mL) was added to a stirred solution of compound **E** (1.5 mmol) in EtOH (30 mL). The mixture was refluxed for 3 h and then neutralized with an 1M HCl solution. The precipitate was obtained by filtration and washed with water several times. Yield: 98%. ^{1}H NMR (400 MHz, DMSO-*d*): δ = 8.13 (m, 3H), 8.01 (d, 2H), 7.97 (m, 8H), 7.83 (d, 2H), 7.74 (d, 2H), 2.25 (s, 2H), 1.04 (s, 9H) ppm.

Synthesis of (*Z*)-*N*1-(2-(4-(4-(2-cyano-2-(4-(4-(3,3-dimethylbutanamido)benzamido)-phenyl)vinyl)benzamido)benzamido)ethyl)ethane-1,2-diaminium (**2**): Compound **F** (0.3 mmol), 1,4-bis-Boc-1,4,7-triazaheptane (0.6 mmol), EDC (0.9 mmol), and DMAP (0.9 mmol) were dissolved in DMF (20 mL). The mixture was stirred at 25 °C for 72 h. The solvent was evaporated under reduced pressure. After addition of water, the crude mixture was filtered and washed with EA. The precipitate was then dissolved in the solution of DCM (20 mL). The mixture was held at 0 °C, and a solution of TFA (5 mL) in DCM (5 mL) was carefully added. The mixture was stirred for 3 h. After evaporating solvents, the resultant solid was washed with THF, DEE, and DCM several times. Yield: 54%.

Chemical characterization of **2**:

^{1}H NMR (400 MHz, DMSO-*d*): δ = 8.13 (m, 3H), 8.07 (d, 2H), 7.98 (m, 4H), 7.92 (m, 4H), 7.82 (d, 2H), 7.75 (d, 2H), 3.57 (m, 2H), 3.19 (m, 6H), 2.25 (s, 2H), 1.05 (s, 9H) ppm.

^{13}C NMR (400 MHz, DMSO-*d*): δ = 171.4, 167.5, 165.58, 143.2, 142.1, 141.4, 139.2, 138.3, 136.7, 129.4, 128.7, 126.9, 120.9, 119.2, 118.8, 116.9, 111.9, 49.6, 48.3, 45.1, 34.5, 32.3, 30.5 ppm.

MS (MALDI-ToF) m/z calculated: 687.84; m/z calculated for $[M+Na]^+$ adduct: 710.83; m/z found: 710.83.

Elemental Analysis calculated (%) for $C_{40}H_{45}N_7O_4$: C 69.85, H 6.59, N 14.25, O 9.30; found: C 69.84, H 6.57, N 14.24.

S3. Sample preparation

Deionized water was added to a sample of **2** and a sonicator bath was used to promote self-assembly. After 24 h post-sonication at room temperature, **2** in its *trans* state in water was observed to form nanoribbons. Nanotubes were obtained by irradiating an aqueous solution of **2** with UV light for 1 h post-sonication. The reverse isomerization (*cis* to *trans*) was obtained by heating the solution at 80 °C for 1 h and cooling slowly to room temperature.

S4. A note on vinylnitrile isomer naming conventions

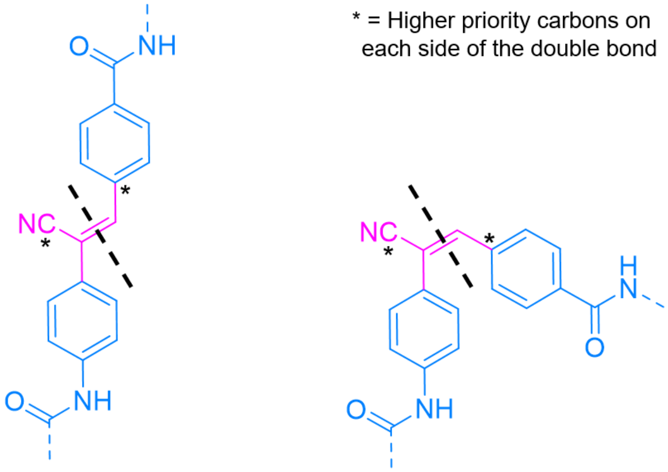

* = Higher priority carbons on
each side of the double bond

(*Z*) isomer **(*E*) isomer**

Figure S2. Naming of vinylnitrile isomers and identification of higher priority carbons on each side of the vinylnitrile double bond.

According to IUPAC naming conventions, the (*Z*) isomer of cyanostilbene should be considered its *cis* isomer because the higher priority carbons fall on the "same side" of the double bond and the (*E*) isomer should be considered the its *trans* isomer because the higher priority carbons fall on "opposite sides" of the double bond. However, the (*Z*) and (*E*) isomers are most frequently labelled in literature as *trans* and *cis*, respectively, because of unintended misnaming as an extension from stilbene isomer identification (e.g. the left molecule in Figure S2 would be *trans* if there were no substitutions on the double bond). For consistency with previous literature, we have chosen to use the colloquial nomenclature; that is, we denote the (*Z*) isomer as *trans* and the (*E*) isomer as *cis*.

S5. Characterization details

Proton (^{1}H) and carbon (^{13}C) nuclear magnetic resonance (NMR) measurements were performed on a Bruker Avance III DPX 400 with samples dissolved in deuterated dimethylsulfoxide (DMSO-*d*). The chemical shifts were measured in parts per million (ppm) downfield from tetramethylsilane.

Molecular weight analysis of final compounds was conducted on a Bruker Omniflex matrix-assisted laser desportion/ionization-time of flight (MALDI-ToF). A matrix solution was prepared by adding 15 mg of α-cyano-4-hydroxycinnamic acid to 1 mL of 1:1 water:acetonitrile by volume with 0.1% TFA, vortexing for one minute, centrifuging for 20 s, and retaining the supernatant. 10 μL of a 1 mg/mL amphiphile solution was then transferred into a centrifuge tube and diluted with the matrix solution to a 50 pmol/μL concentration. 1 μL of a 1 mg/mL calibrant solution (SpheriCal Peptide Low, Polymer Factory) in tetrahydrofuran was added to the solutions as an internal calibrant. 2 μL of the final solution was pipetted and dried onto a sample plate for analysis.

Elemental analysis (EA) of final compounds was determined using a Vario EL elemental analysis (EA) instrument. Three replicate experiments were conducted per compound.

Ultraviolet-visible (UV-Vis) absorption spectra were captured on a JASCO V760 spectrophotometer. 365 nm wavelength UV light used to irradiate samples was produced by an LED Hönle 2.0 Powerpen. UV-Vis solutions were prepared at 0.1 mg/mL.

Small angle X-ray scattering (SAXS) measurements were performed at Beamline 12-ID-B of Advanced Photon Source at Argonne National Laboratory. The X-ray radiation energy was 13.3 keV and a Pilatus 2M detector was employed for data collection. The 2-D X-ray scattering patterns were background subtracted and processed using beamline software for reduction to 1-D data curves. Amphiphile solutions at a 30 mg/mL concentration were used for SAXS measurements.

Transmission electron microscopy (TEM) images were captured on a FEI Tecnai G2 Spirit TWIN microscope at an accelerating voltage of 120 kV. Grids were prepared for TEM experiments by depositing a 7 mg/mL amphiphile solution onto a continuous carbon grid for 10 sec, blotting to remove the solution, depositing a 1% phosphotungstic acid solution onto the grid, and blotting to remove the stain.

S6. Chemical characterization

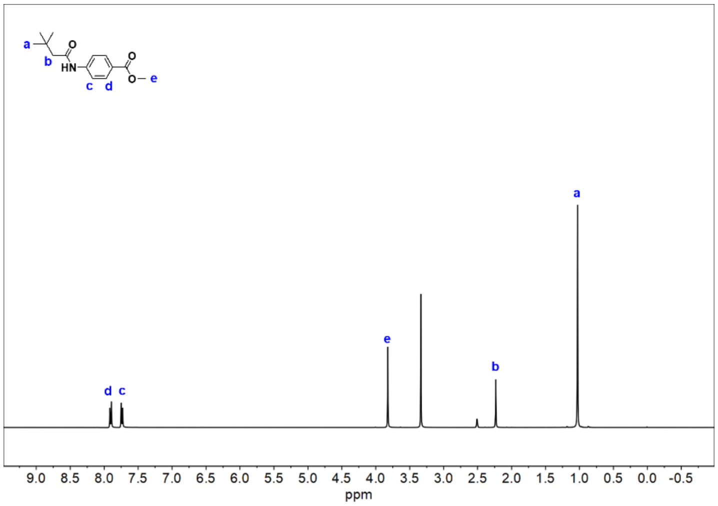

Figure S3. ^{1}H NMR spectra of compound **A**.

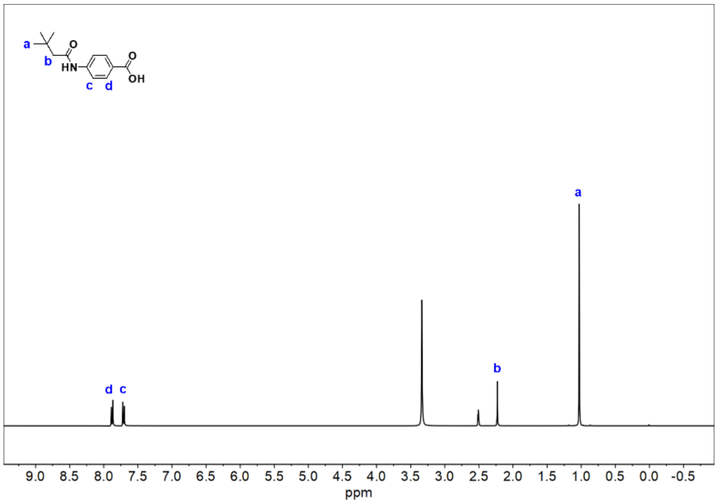

Figure S4. ^{1}H NMR spectra of compound **B**.

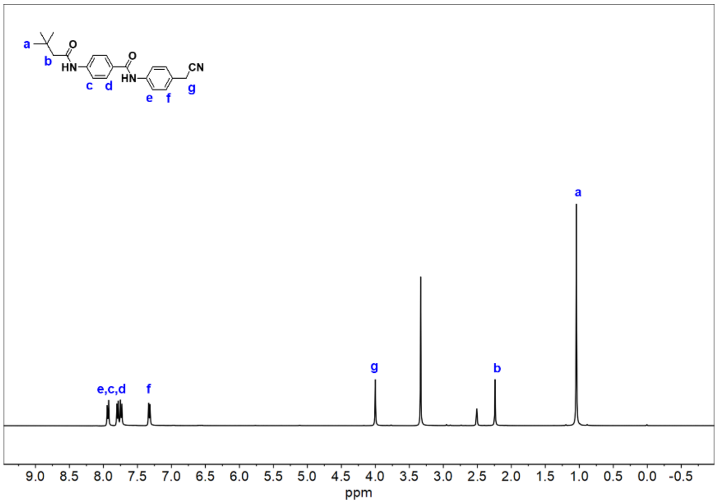

Figure S5. ^{1}H NMR spectra of compound **C**.

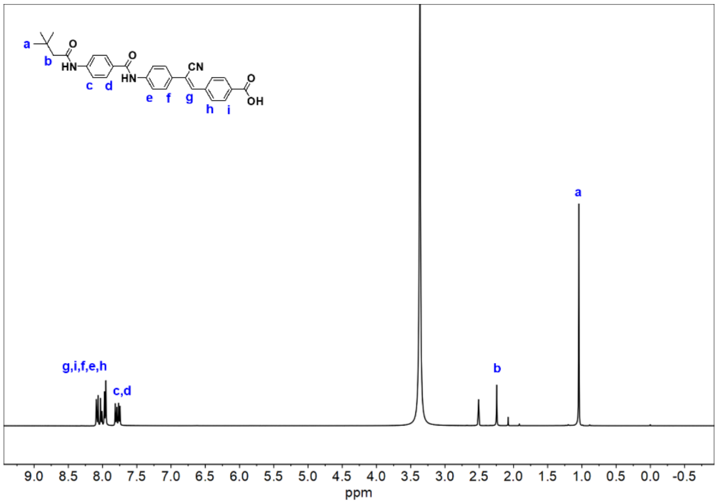

Figure S6. ^{1}H NMR spectra of compound **D**.

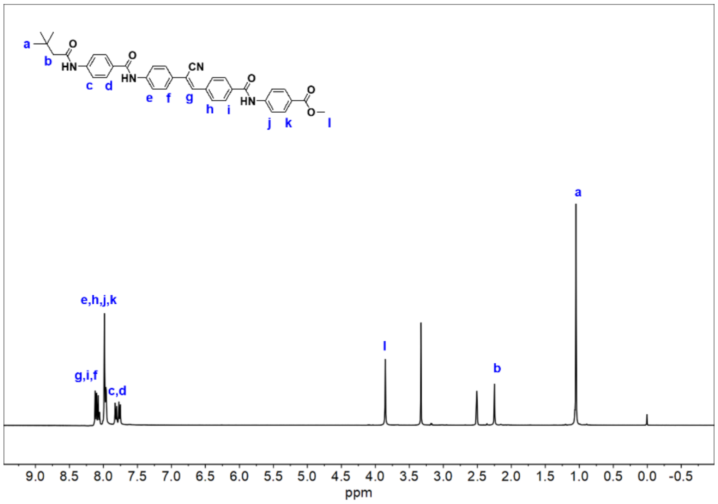

Figure S7. ^{1}H NMR spectra of compound **E**.

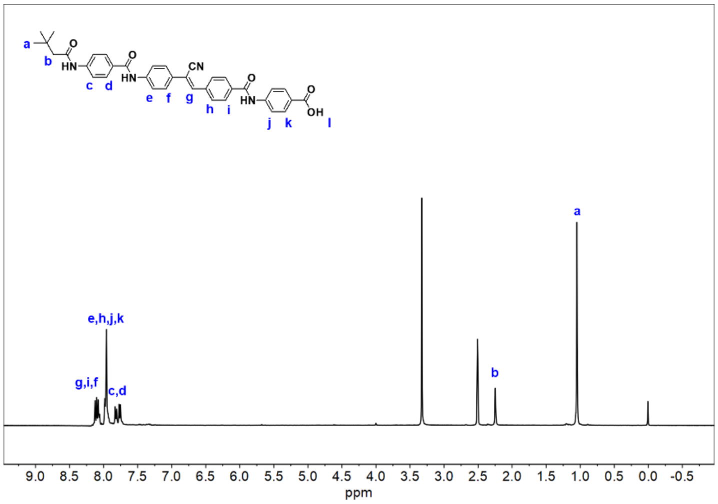

Figure S8. ^{1}H NMR spectra of compound **F**.

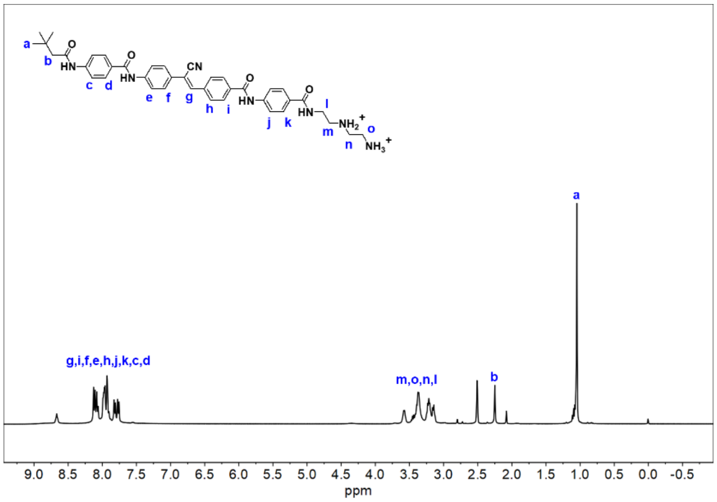

Figure S9. ^{1}H NMR spectra of **2**.

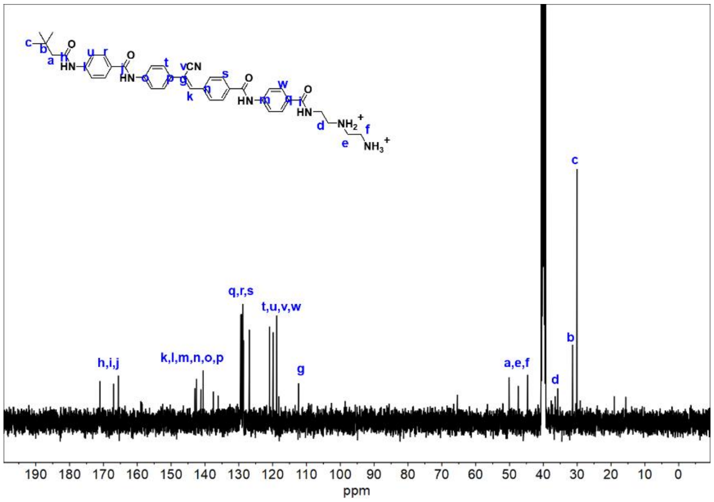

Figure S10. ^{13}C NMR spectra of **2**.

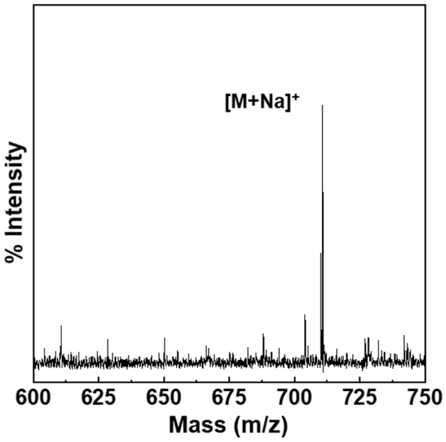

Figure S11. MALDI-ToF mass spectra of **2**. The peak labelled $[M+Na]^+$ corresponds to m/z = 710.83, which matches the expected m/z for **2** of 710.83.

	Calculated Content (wt %)	Experimental Content (wt %)
C	69.85	69.84
		69.83
		69.81
H	6.59	6.57
		6.55
		6.51
N	14.25	14.24
		14.23
		14.19

Figure S12. Elemental analysis of **2** over three replicate runs.

S7. Nanostructure fitting to small angle X-ray scattering profiles

Fitting of SAXS data was completed in SasView software to determine the morphology of compound **1** and **2** nanostructures. Compound **1** was best fit to a lamellar_hg model, which provides separate scattering length densities for the head group and tail (including the structural domain) group. Compound **2** in its initial assembled state was best fit to a rectangular prism model; in its post-UV irradiation state was best fit to a hollow cylinder model; and in its post-annealing state was best fit to a rectangular prism model. The following parameters were used for the fits.

Model Parameter	Value
Head Group Scattering Length Density	9.40×10^{-6} Å^{-2}
Tail Group Scattering Length Density	12.6×10^{-6} Å^{-2}
Solvent Scattering Length Density	9.47×10^{-6} Å^{-2}
Head Group Layer Total Thickness	11.1 Å
Tail Group Layer Thickness	28.0 Å
Background	4.0×10^{-5} cm^{-1}

Figure S13. Parameters for fitting SAXS of compound **1** nanostructures after initial assembly and after annealing to a lamellar model (Figure 2c).

Model Parameter	Value
Scattering Length Density	9.98×10^{-6} Å^{-2}
Solvent Scattering Length Density	9.47×10^{-6} Å^{-2}
Thickness	47.0 Å
Width-to-thickness ratio	1.15
Length-to-thickness ratio	200.0
Distribution of width-to-thickness ratio	1.13
Background	5.0×10^{-4} cm^{-1}

Figure S14. Parameters for fitting SAXS of compound **2** nanostructures after initial assembly to a rectangular prism model (Figure 4a). The distribution of width-to-thickness ratio polydispersity factor is defined as the fraction of the standard deviation of the width-to-thickness ratio to its mean, and follows a Gaussian distribution.

Model Parameter	Value
Scattering Length Density	9.98 x 10^{-6} $Å^{-2}$
Solvent Scattering Length Density	9.47 x 10^{-6} $Å^{-2}$
Core Radius	97.0 Å
Shell Thickness	60.7 Å
Length	1000 Å
Background	7.0 x 10^{-6} cm^{-1}

Figure S15. Parameters for fitting SAXS of compound **2** nanostructures after UV irradiation to a hollow cylinder model (Figure 4c).

Model Parameter	Value
Scattering Length Density	9.98 x 10^{-6} $Å^{-2}$
Solvent Scattering Length Density	9.47 x 10^{-6} $Å^{-2}$
Thickness	47.0 Å
Width-to-thickness ratio	1.2
Length-to-thickness ratio	200.0
Distribution of width-to-thickness ratio	0.55
Background	5.0 x 10^{-4} cm^{-1}

Figure S16. Parameters for fitting SAXS of compound **2** nanostructures after annealing to a rectangular prism model (Figure 5c). The distribution of width-to-thickness ratio polydispersity factor is defined as the fraction of the standard deviation of the width-to-thickness ratio to its mean, and follows a Gaussian distribution.

S8. Statistical topographical analysis of nanoribbon contours

Sample preparation: A solution of compound **2** nanoribbons was prepared for atomic force microscopy (AFM) analysis by sonicating for 24 h at room temperature at 30 mg/mL and diluting to a final concentration of 0.03 mg/mL. This solution was deposited onto a glass substrate which was cleaned with DI water and ethanol, dried with N_2 (g), and activated with a UV/ozone treatment. The solution was incubated for 5 min, and then rinsed off with DI water and dried with a N_2 stream prior to AFM imaging.

AFM imaging: Images of compound **2** nanoribbons were captured in tapping mode in ambient air on a Bruker/JPK Nanowizard 4 AFM. Olympus AC160TS-R3 cantilevers were used, with a nominal spring constant of 26 N m^{-1} and a resonance frequency of approx. 300 kHz 512 x 512 pixel AFM images were produced at a 3–10 Hz scanning speed. A representative AFM image is shown in Fig. S17.

Statistical topographical analysis: Nanoribbon shape fluctuations were extracted from AFM images and statistically processed using Easyworm software.[34] In this study, the software was used to produce parametric splines from the contours of n = 96 nanoribbons. These parametric splines record coordinates of all knots along the ribbons, and each combination of knots is analyzed to obtain a secant length L from which the midpoint of the secant deviates from the nanoribbon contour by the distance δ. A persistence length P is subsequently extracted via a least-squares fitting a worm-like chain model for semi-flexible polymers to the data, which relates the mean-square of δ to the secant length L according to: $< \delta^2 > = L^3/(48 \times P)$. Thus, a higher persistence length corresponds to a smaller orientation change over a given distance along a nanoribbon's contour. The flexural rigidity F is calculated using $F = P \times k_B T$, where the persistence length is scaled by thermal energy. Using this, the Young modulus E is obtained by dividing the flexural rigidity by the nanoribbon's area moment of inertia, $E = F/I$. We use the AFM height of d= 3.2 ± 0.8 nm as the nanoribbon diameter in calculating the moment of inertia, $I = \pi \cdot d^4/64$, as in our previous study.[30]

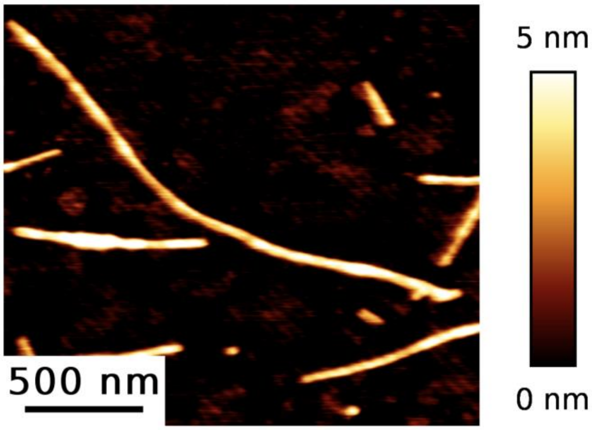

Figure S17. Representative AFM image of compound **2** nanoribbons used for statistical topographical analysis to determine nanoribbon stiffness.

S9. UV-Vis spectroscopy controls and experiments

Compound **1**, a conventional AA with no photoswitching group installed in the structural domain, shows no response to UVA irradiation for 1 h, as shown in Figure S18.

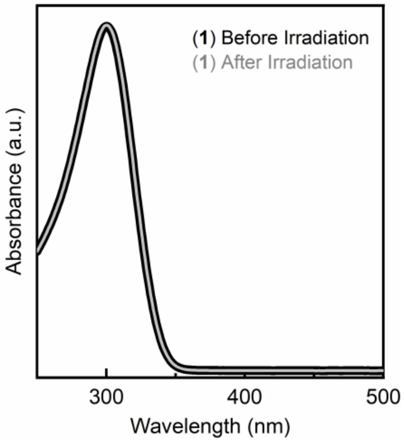

Figure S18. Compound **1** nanoribbon solution irradiated with UVA light for 1 h shows no change in UV-Vis absorbance.

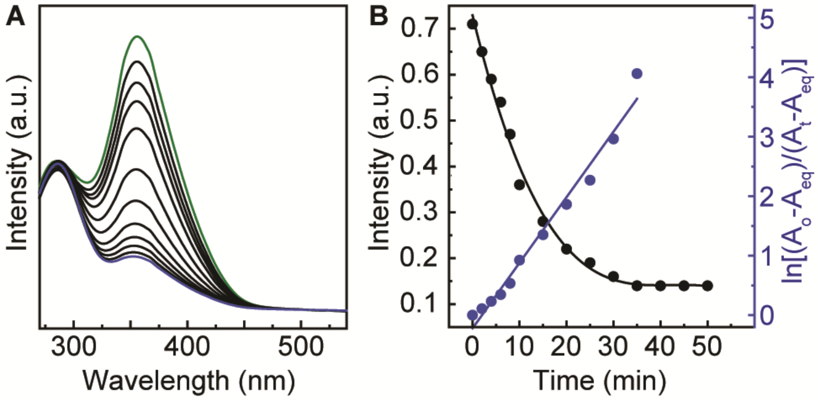

Figure S19. (a) UV-Vis spectra of compound **2** dissolved in DMSO with over 50 min of irradiation with UVA light irradiation. The initial state is the green line, and the final state is the blue line. (b) Time-dependent absorbance changes are used to calculate a photoisomerization rate constant of $K = 1.10 \times 10^{-1}$/min of compound **2** in DMSO.

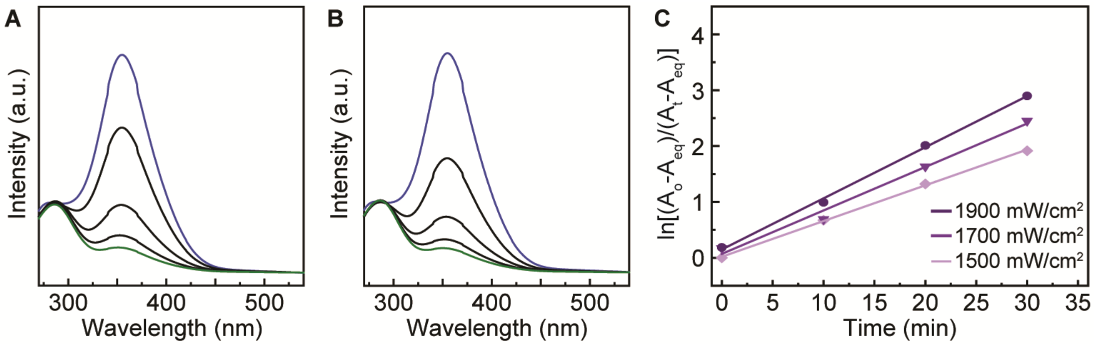

Figure S20. (a) Time-dependent UV-Vis spectra of compound **2** under medium intensity UVA light (1700 mW/cm^2; initial line in blue, final line in green). (b) Time-dependent UV-Vis spectra of compound **2** under high intensity UVA light (1900 mW/cm^2; initial line in blue, final line in green). (c) From a first-order plot of the *trans* to *cis* isomerization of compound **2** at each irradiation power level, we extract photoisomerization rate constants of 5.44 × 10^{-2}/min, 7.77 × 10^{-2}/min, and 9.15 × 10^{-2}/min for irradiation powers of 1500 mW/cm^2, 1700 mW/cm^2, and 1900 mW/cm^2, respectively.

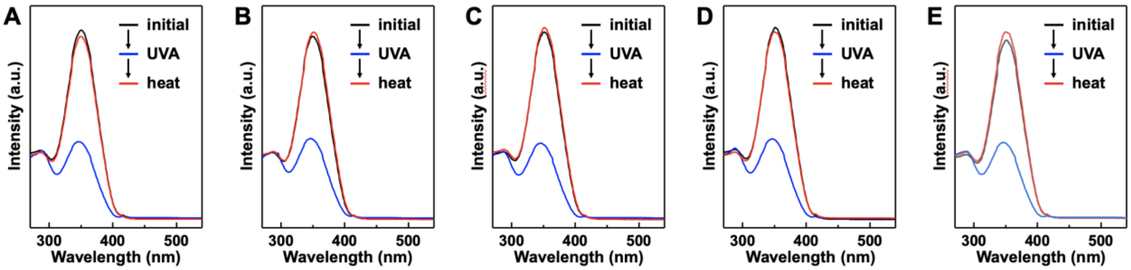

Figure S21. UV-Vis spectra of compound **2** in water initially, after UVA irradiation, and after annealing over five cycles: (a) cycle one, (b) cycle two, (c) cycle three, (d) cycle four, and (e) cycle five. The recovery of the absorbance to its initial state after annealing suggests that little to no photobleaching occurs during this process.

S10. Probing for the Tyndall effect in the *trans* and *cis* states of compound 2

Atomic force microscopy (AFM) images which complement the investigation into the Tyndall effect in Figure S22 were recorded on a Park Systems NX10. A 7 mg/mL solution of **2** after self-assembly in water was diluted to 0.01 wt. %, and then a 50 µL droplet solution was deposited onto a freshly cleaned substrate. This substrate was prepared through a plane cleavage of mica, and cleaning with water several times. A PPP-NCHR non-contact cantilever was utilized to produce these images.

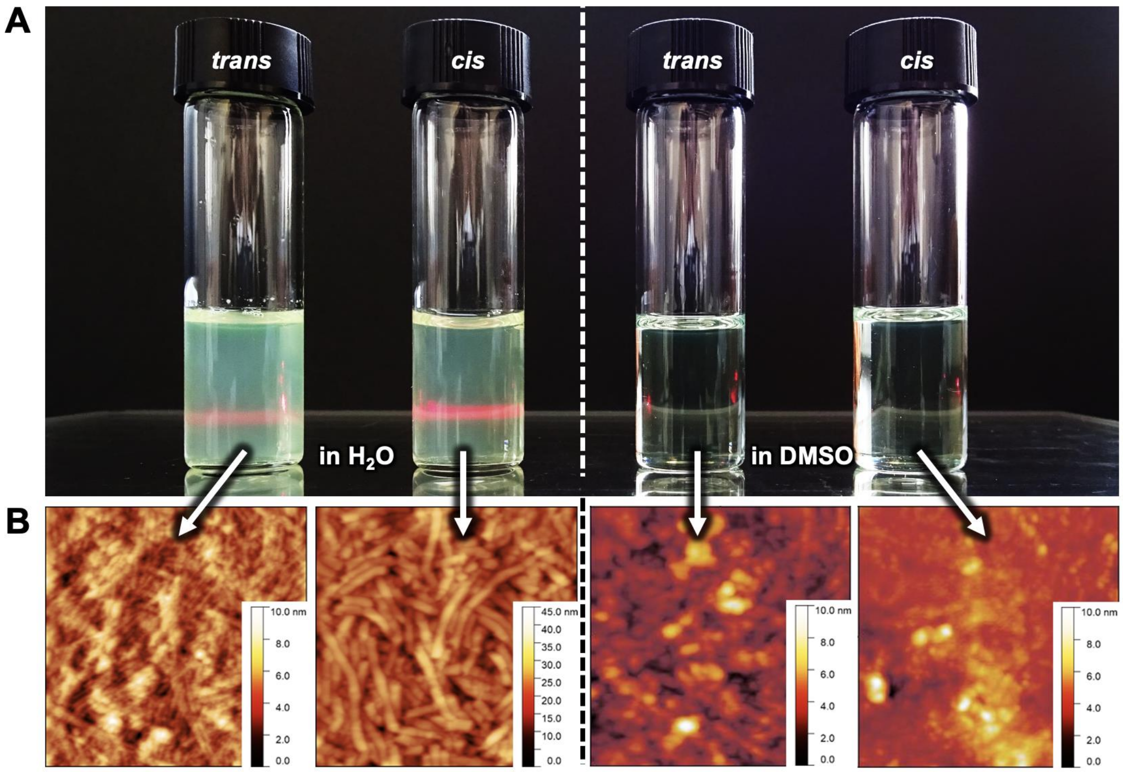

Figure S22. (a) Observation of the Tyndall effect of 7 mg/mL solutions of compound **2** in water (left two vials) or DMSO (right two vials) in its *trans* or *cis* state. The scattering observed by compound **2** in water is indicative of the maintenance of a nanostructure; its absence in DMSO indicates that compound **2** does not form an ordered nanostructure. (b) AFM micrographs of the solutions from each vial indicate show, from left to right, nanoribbons from the assembly of compound **2** in water in its *trans* state; nanotubes following the irradiation of compound **2** in water into a *cis*-rich state; and no ordered nanostructure when compound **2** is dissolved in DMSO in either its *trans* or *cis* states.

S11. Packing of compound 2 into nanoribbons and nanotubes

One dimensional (1D) wide-angle X-ray diffraction (WAXD) experiments were conducted on a Bruker D8 Discover using Cu Kα radiation. The diffraction peak positions and widths were calibrated with crystalline silicon powder. Background scattering was subtracted from the samples using instrument software. 30 mg/mL solutions of compound **2** nanoribbons and nanotubes were lyophilized for WAXD analysis.

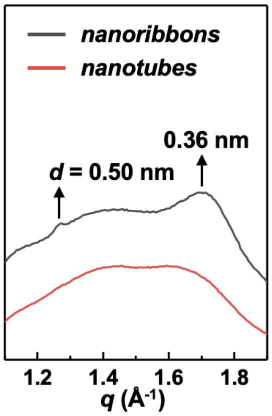

Figure S23. 1D WAXD pattern of lyophilized compound **2** nanoribbons and nanotubes. The geometries of these nanostructures are observed to retain their shape when dried by AFM.